Identifying the Optimal Pd Ensemble Size in Dilute PdAu Alloy Nanomaterials for Benzaldehyde Hydrogenation

Selina K. Kaiser, Jessi E. S. van der Hoeven, George Yan, Kang Rui Garrick Lim, Hio Tong Ngan, Sadhya Garg, Mustafa Karatok, Michael Aizenberg, Joanna Aizenberg, Philippe Sautet,* Cynthia M. Friend,* and Robert J. Madix*

Read Online

ACCESS | Metrics & More | Article Recommendations | Supporting Information

ABSTRACT: Unraveling metal nuclearity effects is central for active site identification and the development of high-performance heterogeneous catalysts. Herein, a platform of nanostructured palladium (Pd) in gold (Au) dilute alloy nanoparticles supported on raspberry-colloid-templated (RCT) silica was employed to systematically assess the impact of the Pd ensemble size for the low-nuclearity regime in the Au surface layer, from single atoms to clusters, on the catalytic performance in the liquid-phase hydrogenation of benzaldehyde to benzyl alcohol. Combining catalyst evaluation, detailed characterization, and mechanistic studies based on density functional theory, we show that Pd single atoms in the Au surface plane (corresponding to samples with 4 atom % Pd in Au) are virtually inactive in this reaction and benzyl alcohol production is optimal over small Pd clusters (corresponding to samples with 10−12 atom % Pd in Au) due to superior benzaldehyde adsorption and transition state stabilization for the C−H bond formation step. For larger Pd ensembles (samples with ≥10 atom % Pd in Au), C−O bond hydrogenolysis occurs, promoting toluene formation and decreasing the selectivity toward benzyl alcohol, in line with a relatively lowered C−O bond cleavage barrier. Nevertheless, the nanostructured bimetallic $Pd_{13}Au_{87}/SiO_2$-RCT catalyst still outperforms monometallic Pd counterparts in terms of selectivity for benzyl alcohol over toluene at comparable conversion and rate. Furthermore, the stability is improved compared to pure Pd nanoparticles due to inhibited particle agglomeration in the RCT silica matrix.
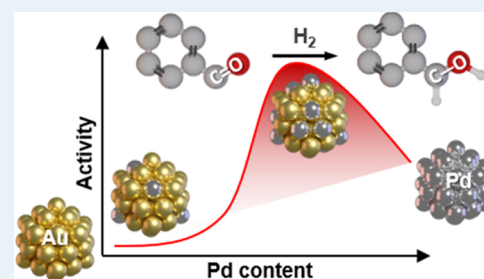
KEYWORDS: hydrogenation, dilute alloy, ensemble size, gold, palladium, density functional theory, heterogeneous catalysis

INTRODUCTION

Currently, more than 80% of all catalytic processes in the industry employ heterogeneous catalysts, which are most commonly based on metals.[1] Within this class of catalysts, intermetallic compounds or metal alloys are of particular interest due to their diverse reactivity and the potential to open up new catalytic performance.[2] To explore these possibilities in a systematic manner, nanostructured dilute binary alloys, comprised of a well-defined active metal species incorporated into a second less active yet catalytically selective metal, are powerful model systems to derive structure−performance relationships. Catalytic hydrogenation is an application of particular relevance, as more than 25% of all chemical transformations require at least one such step.

Currently, many hydrogenations rely on the use of homogeneous catalysts under a hydrogen atmosphere or the use of stoichiometric amounts of metal hydrides. From economical and environmental footprint points of view, the development of heterogeneous catalysts for these reactions is highly desirable due to the simplified product separation, catalyst recyclability, and waste minimization.[3] Recently, alloy catalysts presenting a range of ensemble sizes for the active metal—from a single atom to clusters[4−6]—which can be

regarded as a link between traditional heterogeneous and homogeneous catalysts, have shown promise for the selective hydrogenation of various alkynes to alkenes compared to traditional nanoparticle-based catalysts.[2,7−11] Extending the applicability of these nanostructured alloys to aldehyde hydrogenation is highly desirable for the sustainable production of alcohols in the bulk in fine chemical and pharmaceutical industries.[12]

An emerging material class, combining the advantages of well-defined metal alloys with high thermal and catalytic stability, is raspberry-colloid-templated (RCT) catalysts.[13,14] By exploiting the self-assembly of sacrificial organic colloids bearing metal nanoparticles on their surface (termed raspberry particles) in the presence of oxide matrix precursors, highly stable porous networks can be synthesized into which these
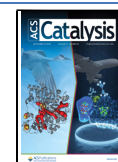
dilute binary alloy nanoparticles can be embedded. Herein, the hydrogenation of benzaldehyde to benzyl alcohol, which is broadly employed as a specialty chemical[15] and which mimics chemical motifs typically found in biomass-derived oxygenates, is reported over a series of PdAu/SiO$_2$-RCT catalysts.

■ EXPERIMENTAL SECTION

Catalyst Synthesis. *Chemicals.* All chemicals were used as received without further purification. Hydrogen tetrachloroaurate trihydrate (HAuCl$_4$·3H$_2$O, ≥99.9%), sodium borohydride (NaBH$_4$, 99%), sodium tetrachloropalladate (Na$_2$PdCl$_4$, ≥99.99%), sodium citrate tribasic dihydrate (≥99.0%), L-ascorbic acid (≥99.0%) poly(vinylpyrrolidone) (PVP, M_w 55000 g/mol), and tetraethyl orthosilicate (TEOS, 98%) were purchased from Sigma-Aldrich. Absolute ethanol (EtOH) was purchased from KOPTEC. Ultrapure water (Millipore Milli-Q grade) with a resistivity of 18.2 MΩ cm^{-1} was used in all of the experiments. All glassware for nanoparticle syntheses were cleaned with fresh aqua regia (HCl/HNO$_3$ in a 3:1 volume ratio), rinsed with large amounts of water, and dried at 403 K before usage.

Gold Nanoparticles. Following the procedure adapted from Grabar et al., monodisperse gold nanoparticles were synthesized.[16] Accordingly, 20 mg of HAuCl$_4$ dissolved in 1 mL of Milli-Q (MQ) water was added to 200 mL of MQ water in a 500 mL round bottom flask. The reaction mixture was kept under magnetic stirring (400 rpm), followed by the addition of 1.0 mL of a trisodium citrate solution (50 mg of sodium citrate dihydrate per 2.0 mL of H$_2$O). The reaction mixture was left to stir for ten minutes at room temperature. Subsequently, 100 μL of aqueous NaBH$_4$ (9.0 mg NaBH$_4$ in 1.0 mL of cold H$_2$O) was added to the remaining 1.0 mL of trisodium citrate. The combined mixture was then rapidly added to the reaction under increased stirring (700 rpm), causing the solution color to instantly change from yellow to dark purple. After wrapping the flask in aluminum foil to reduce light exposure, the reaction mixture was left to stir overnight at room temperature, causing a final color change to red.

Pd Overgrowth. To grow palladium on the previously synthesized gold nanoparticles, 75 mL of aqueous PVP solution (0.1 g of PVP per mL of H$_2$O) was first added to 250 mL of citrate-stabilized gold nanoparticles under continuous stirring (400 rpm). After 30 min, 2.5 mL of 0.1 M HCl was added to the reaction and left to stir for additional 30 min. Subsequently, 150 μL of 10 mM Na$_2$PdCl$_4$ and 150 μL of 40 mM ascorbic acid were sequentially added (with a 5 min interval between additions) to a vigorously stirring mixture to obtain the Pd$_4$Au$_{96}$ NPs. Likewise, for Pd$_8$Au$_{92}$, Pd$_{10}$Au$_{90}$, and Pd$_{13}$Au$_{87}$, 300, 450, and 670 μL of 10 mM Na$_2$PdCl$_4$ and 40 mM ascorbic acid were added, respectively. The reaction flask was covered with aluminum foil to reduce light exposure and the mixture was left to react overnight. Ultraviolet−visible (UV−vis) spectra were recorded the following day and samples were stored in the dark until use.

Raspberry Colloids. The gold−palladium nanoparticles were attached to the sacrificial polystyrene (PS) colloids (d_{PS} = 374 nm) to generate the raspberry colloids. Accordingly, 240 mL of the nanoparticle dispersion was added dropwise under continuous stirring at 400 rpm to 13.8 mL of amidine-functionalized PS colloids (8.7 wt % in water) over 1 h, followed by the addition of 1.5 mL of 0.1 M HCl to lower the pH to ∼4. The raspberry colloids were left to stir for 30 min before washing with MQ water three times using centrifugation

(12,000g, 35 min) and subsequently redispersed in 24 mL of MQ water (∼5 wt % raspberry colloids in water).

RCT Preparation. A total of three 4 mL aliquots of the raspberry colloid dispersion (∼5 wt % in water) were dried in three separate conical vials at 338 K in air to yield a colloidal crystal. To each vial, ∼200 μL of prehydrolyzed TEOS solution (33 vol % of 0.10 M HCl in MQ H$_2$O solution, 33 vol % ethanol, 33 vol % TEOS) was infiltrated into the colloidal crystal, followed by drying at 338 K for 1 h. This step was repeated 3 times. The samples were calcined to remove sacrificial PS templating colloids by heating them in static air, ramping the temperature from room temperature to 773 K over 5 h and then maintaining the temperature at 773 K for 2 h, before cooling to room temperature over 3−4 h.

Catalyst Characterization. Bright-field transmission electron microscopy (TEM) images were acquired using a JEOL 2100 microscope (Japan) with an operating voltage of 200 kV. High-angle annular dark-field scanning transmission electron microscopy (HAADF-STEM) and energy-dispersive X-ray spectroscopy (EDX) were performed using a JEOL ARM 200F STEM equipped with a cold field emission gun (FEG, operated at 200 keV) and an integrated aberration corrector (Cs). The samples were dispersed in absolute ethanol and drop-cast onto a Formvar/Carbon 200 mesh copper grid (Ted Pella). Scanning electron microscopy (SEM) images were acquired using a Zeiss Ultra55 field-emission scanning electron microscope (FESEM). Inductively coupled plasma mass spectrometry (ICP-MS; Thermo Fisher Scientific, iCAP RQ) was used for compositional analysis (metal composition and metal weight loading). The catalysts were digested using aqua regia at 313 K for 72 h. Gold and palladium calibration solutions were prepared just before analysis by dilution standard solutions of HAuCl$_4$ (1000 ppm in 2% HNO$_3$) and Pd(NO$_3$)$_2$ (1000 ppm in 2% HNO$_3$) in 1.4% HNO$_3$ (aq), respectively. *Ex situ* X-ray photoelectron spectroscopy (XPS) analyses were performed to identify surface elements and describe the surface composition with a Thermo Fisher K-α+ X-ray photoelectron spectrometer equipped with an Al source, 180° double-focusing hemispherical analyzer, and 128-channel detector. Samples were analyzed using monochromatic Al Kα radiation (1486.6 eV, generated by a 12 kV electron beam) focused onto a 400 μm spot size, and the flood gun was switched on throughout the analysis. Binding energies were first calibrated using the adventitious C 1s peak, taken to be 284.8 eV. The Au 4f$_{7/2}$ and Pd 3d$_{5/2}$ spectra were fitted with modified Doniac−Sunjic functions, after Shirley background subtraction, using Au/SiO$_2$ and Pd/SiO$_2$ as reference samples. The selected peak positions of the different gold and palladium species are based on the literature reported data[5] and fixed with an error of ±0.1 eV.

Temporal Analysis of Products. The O$_2$ titration experiments were carried out in a modified commercial TAP-2-type reactor.[17] The Pd$_8$Au$_{92}$ (9.5 mg), Pd$_{10}$Au$_{90}$ (5.6 mg), and Pd$_{13}$Au$_{87}$ (5.9 mg) catalysts were sieved to 100−300 μm and then sandwiched in a thin zone configuration between two layers of inert SiC particles (∼350 μm) in a quartz microreactor. Details on the TAP microreactor can be found elsewhere.[18] After loading into the microreactor, the catalysts were pretreated for the initial oxidation with dry air (Airgas, AI-D300, 20−22% of O$_2$ in N$_2$) in flow mode (∼40−45 cm^3 min^{-1}) at 673 K for 30 min and then cooled to 553 K in flowing air. The microreactor was evacuated to 10^{-8} Torr before the O$_2$ titration experiments. The amount of oxygen

species was determined by titration with a sequence of quantified pulses of 20.84 mol % CO/Ar mixture (containing $\sim 2 \times 10^{14}$ molecules of CO in each pulse) until CO_2 production had ceased. Details on the quantification of oxygen on the surface of the PdAu-RCT-SiO$_2$ catalysts can be found elsewhere.[18] The method for estimating the number of surface atoms, which is used to calculate the surface Pd fraction on the PdAu alloy nanoparticles, is described in the Supporting Information.

Catalytic Evaluation. Liquid-phase flow benzaldehyde hydrogenation was carried out in a continuous flow fixed-bed reactor (HEL FlowCat). The catalyst (W_{cat} = 10−40 mg, sieved into particles of 100−300 μm) was mixed with quartz sand (vol/vol 1:5) to achieve a total volume of 2 mL and transferred to a stainless steel reactor tube (6 mm diameter, 150 mm length). A thermocouple with the tip positioned in the center of the catalyst bed was used to maintain the temperature during the reaction at T_{bed} = 323 K. In a typical test, a solution of benzaldehyde (0.5 M, Sigma-Aldrich, 97%) and o-xylene (internal standard, 0.2 M, Sigma-Aldrich, 99%) in isopropanol (Acros Organics, 99.5%) was fed via mass-flow controllers at 0.05 mL min^{-1} from the top into the reactor concurrently with 50 mL STP min^{-1} hydrogen (Airgas, ultrahigh purity grade) at a pressure of 5 bar maintained by a computer-controlled back-pressure regulator. Liquid samples were collected periodically, after a stabilization period of 120 min (60 min of flow equilibration and 60 min of reaction stabilization time), following the previous 60 min. of wetting in isopropanol. The reaction products were analyzed ex situ by gas chromatography-MS (GC-MS) (Agilent Column HP-Plot/Q). To ensure the absence of mass transfer limitations, the dimensionless moduli of Carberry and Weisz−Prater were evaluated and found within the acceptable range (Ca = 0.03; Φ = 0.0005). This is further corroborated by the reproducibility of catalytic experiments, which were successfully reproduced 3 times. To assess the influence of the internal standard (o-xylene) on benzaldehyde hydrogenation, we ran a test in the presence and absence of o-xylene in batch mode. The results were found comparable, verifying o-xylene as a suitable internal standard (Figure S15).

Reaction kinetics of benzaldehyde hydrogenation over selected catalysts were studied at conversion levels <20% in the temperature and pressure range of 323−353 K and 5−10 bar with benzaldehyde concentrations of 0.1−0.5 M to determine the apparent activation energy (E_A) and the partial reaction order of the reactants ($n(H_2)$, $n(BA)$).

The catalytic conversion of benzaldehyde, $X(BA)$, was calculated according to eq 1

$$X(BA),\ \% = \frac{n_{BA}^{inlet} - n_{BA}^{outlet}}{n_{BA}^{inlet}} \cdot 100 \tag{1}$$

where n_{BA}^{outlet} and n_{BA}^{inlet} denote the molar flows of benzaldehyde at the reactor outlet and inlet, respectively. The selectivity S_j of product j (j: benzyl alcohol, toluene, acetal) to the products was calculated according to eq 2

$$S_j,\ \% = \frac{n_j^{outlet} \cdot \nu_{BA,j}}{\sum n_j^{outlet} \cdot \nu_{BA,j}} \cdot 100 \tag{2}$$

where n_j^{outlet} is the molar flow of the product j at the reactor outlet, while $\nu_{BA,j}$ is the stoichiometric coefficient relating the consumption of benzaldehyde and the formation of product j.

The space−time yield (STY) was determined according to eq 3

$$STY,\ mmol_{BOH}\ s^{-1}mol_{Pd}\ ^{-1} = \frac{n_{BOH}^{outlet}}{n_{Pd}} \tag{3}$$

where n_{Pd} denotes the total amount of palladium metal in moles, as determined by ICP-MS.

The reaction rate constant, k, and reaction rate, r, were determined according to eqs 4 and 5, respectively

$$k,\ mmol_{BA}s^{-1}\ mol_{Pd}\ ^{-1} = \frac{n_{BA}^{inlet} - n_{BA}^{outlet}}{n_{Pd}} \tag{4}$$

$$r,\ mmol_{BA}s^{-1}\ g_{cat}\ ^{-1} = \frac{n_{BA}^{inlet} - n_{BA}^{outlet}}{m_{cat}} \tag{5}$$

where m_{cat} denotes the amount of catalyst in grams. After the tests, the reactor was quenched to room temperature in Ar (Airgas, ultrahigh purity grade) flow and the catalyst was retrieved for further characterization.

Liquid-phase batch benzaldehyde hydrogenation was conducted in a 50 mL stainless-steel batch reactor (Parr 5512 with Parr 4848 Controller). In a typical reaction, benzaldehyde (50 mM) and o-xylene (internal standard, 20 mM) were mixed with isopropanol (solvent) to a final volume of 32 mL. Thereafter, 5−20 mg of the same sieved catalyst was added to the solution mixture. The reactor was assembled, stirred at 1000 rpm, and purged four times with N$_2$ gas (99.998%, approx. 30 bar). The reactor was then pressurized 3 times with 20 bar of H$_2$ gas (99.999%) to saturate the reaction solution with H$_2$ and then heated to 150 °C, and the reaction time was set to t = 0. The heated reactor was depressurized to 20 bar H$_2$ once the desired temperature was reached. The reactor was left stirring for 24 h and sample aliquots (approx. 0.2 mL each) were withdrawn at specified timepoints from the reactor's sampling valve and analyzed by ex situ GC-MS using an Agilent HP-1MS column. After each sample withdrawal, the reactor was repressurized back to 20 bar H$_2$.

Density Functional Theory. Density functional theory calculations were performed using Vasp version 5.4.1.[19−21] The exchange−correlation energy was calculated using the Perdew−Burke−Ernzerhof (PBE) functional.[22] Spin polarization was used in all calculations. The projector-augmented wave (PAW) method was used to describe the core electrons.[23,24] The one-electron wavefunctions were expanded using a set of plane waves with a kinetic energy of up to 400 eV. The dDsC dispersion correction method was used to account for the van der Waals interaction between the aromatic ring and the catalyst surface.[25,26] Structural relaxation for reaction intermediates was performed using the conjugate gradient algorithm. Transition states were first searched using the nudged elastic band (NEB) and climbing image (CI) NEB algorithms.[27,28] The highest energy image of each CI-NEB calculation was then refined using the Dimer and quasi-Newton algorithms.[29] The electronic structure in each self-consistent field (SCF) cycle was considered converged when the difference of total energy in consecutive steps falls below 10^{-6} eV. Atomic positions were considered converged when the Hellmann−Feymann forces on unconstrained atoms fell below 0.02 eV/Å.

To simulate the Pd/Au alloys, a (4 × 4) supercell of Au(111) with 4 Au layers was used to represent the catalyst
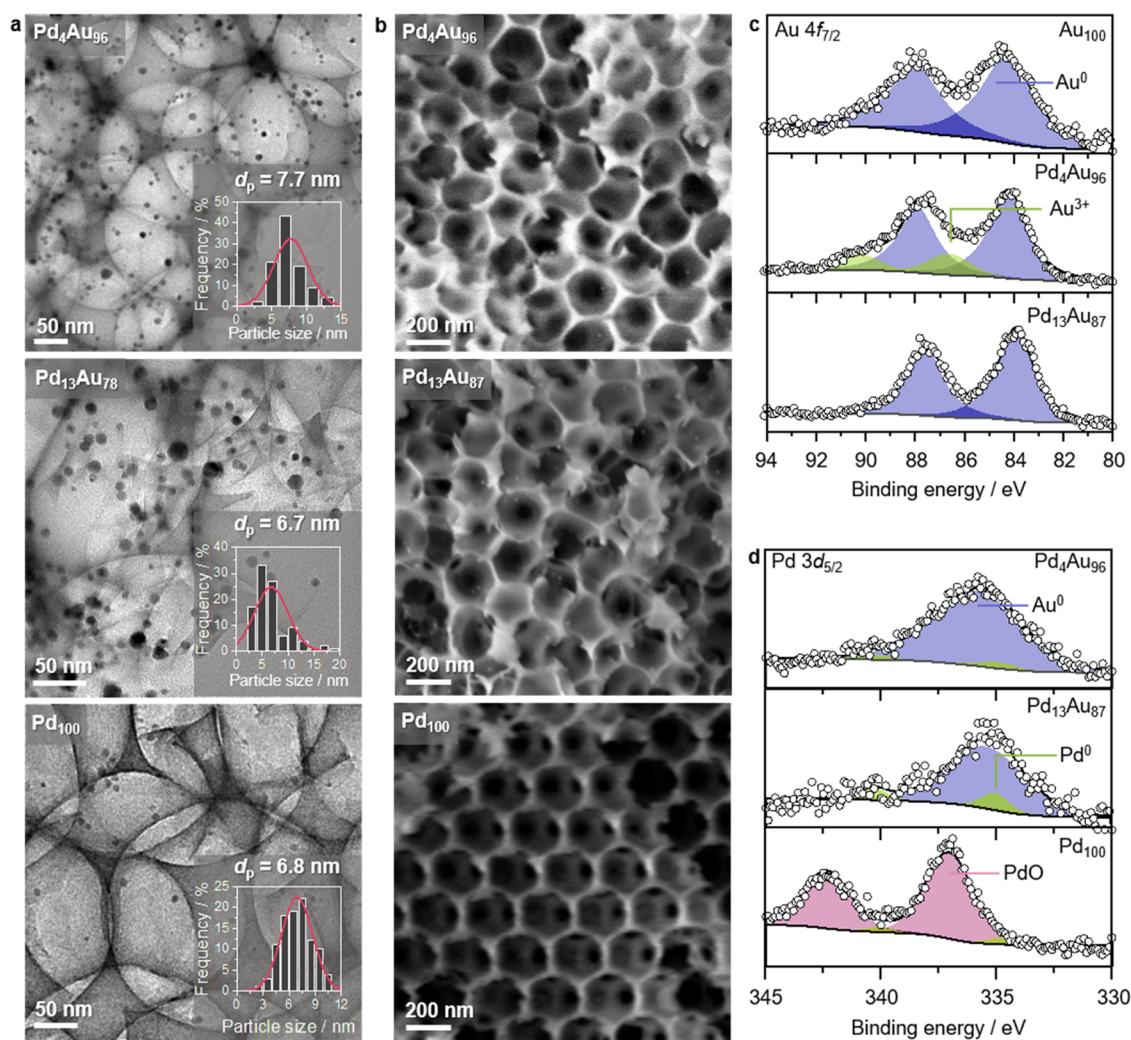
Figure 1. Characterizations of the as-prepared catalysts. (a) Transmission electron microscopy (TEM) images of raspberry-colloid-templated (RCT) Pd_4Au_{96}, $Pd_{13}Au_{78}$, and Pd_{100} nanoparticles embedded into silica pore walls indicate comparable average metal particle sizes and distributions in all samples. (b) Scanning electron microscopy (SEM) images showing the macroporous structure of the support typical for RCT-based catalysts, exemplified here for Pd_{100}, Pd_4Au_{96}, and $Pd_{13}Au_{87}$. (c, d) X-ray photoelectron spectra (XPS) of the Au 4f and Pd 3d regions, suggesting predominantly zero (metallic) oxidation state of Au and Pd in the alloy samples and Pd oxide in Pd_{100}.

surface. Atoms in the bottom two layers of the surface were fixed to their bulk positions, while the top two layers and adsorbates were allowed to relax. Surface Pd ensembles were generated by replacing 1−3 surface Au atoms with Pd. For these structures, the Brillouin zone was sampled using a $(5 \times 5 \times 1)$ mesh centered at the Γ point.[30] Benzaldehyde hydrogenation and deoxygenation were also simulated over the Pd(111) surface. In these calculations, a (4×4) supercell of Pd(111) with 4 Pd layers was used as the catalyst surface. Atoms in the bottom two layers of the Pd(111) slab were fixed to their respective bulk positions. The Brillouin zone of Pd(111) was sampled using a $(5 \times 5 \times 1)$ mesh centered at the γ point.

RESULTS AND DISCUSSION

Synthesis and Characterization of the PdAu/SiO₂-RCT Catalyst Platform. To systematically assess the relationship between the Pd ensemble size in AuPd alloys and the catalytic performance in benzaldehyde hydrogenation, a platform of well-defined RCT catalysts was employed. Uniform alloy nanoparticles homogeneously distributed at the pore walls of

Table 1. Metal Loading in the Catalysts Determined by ICP-MS

catalyst	Pd content (atom %)	total metal loading (wt %)
Pd_4Au_{96}	4.3	2.6
Pd_8Au_{92}	8.5	2.6
$Pd_{10}Au_{90}$	10.5	2.8
$Pd_{13}Au_{87}$	13.5	2.7
Pd_{100}	100	0.4
Au_{100}	0	3.8

highly ordered macroporous silica frameworks were generated. These catalysts were calcined in a static air mixture at 773 K, which draws Pd to the surface.[10] This approach enables tuning the atomic Pd/Au ratio at the surface of the as-prepared alloys, without altering any other potential catalytic descriptors, such as the alloy particle size and density, the metal content, the micro- and macroporosity, and the support structure, thus presenting ideal model systems to derive structure−function correlations. Additionally, these RCT catalysts ensure optimal mass transport, thanks to their robust, macroporous support structure, and they exhibit high thermal and mechanical
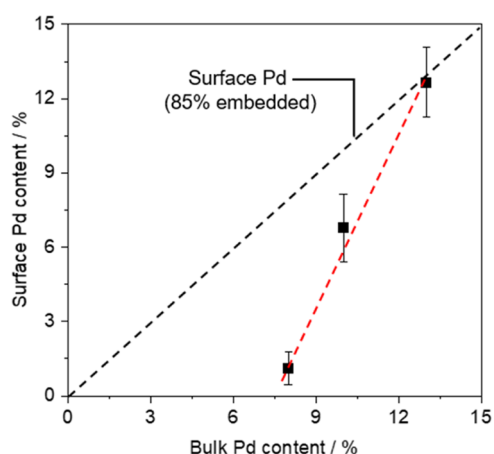
Figure 2. Oxygen titration results indicating the Pd surface composition. The surface Pd composition of oxygen-pretreated PdAu alloy catalysts (dashed red line), determined using quantified pulses of CO from a temporal analysis of products (TAP) reactor, suggests the predominant presence of Pd single atoms in Pd_8Au_{92} and an appreciable presence in $Pd_{10}Au_{90}$. On the contrary, $Pd_{13}Au_{78}$ exhibits mainly Pd ensembles, as indicated by the comparable surface Pd content between the TAP experiments and the expected values (black dashed line) based on ICP-MS.
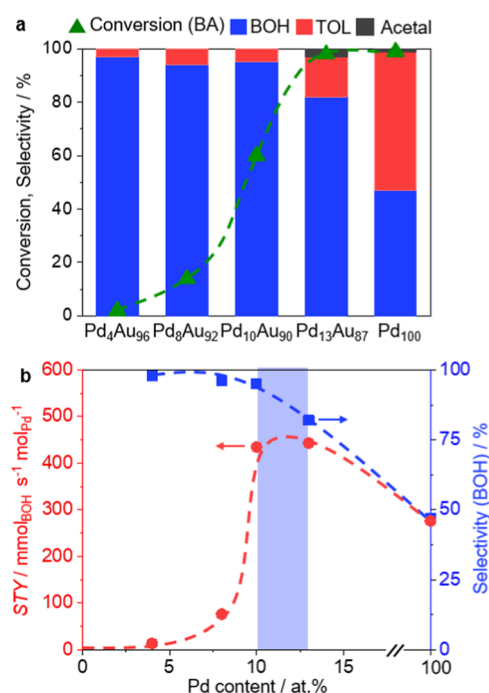
Table 2. Space−Time Yields and Selectivity to BOH of Selected Catalysts

catalyst	STY^a ($mmol_{(BOH)}$ s^{-1} $mol_{(Pd)}^{-1}$)	selectivity (BOH) (%)
Pd_4Au_{96}	13	98
Pd_8Au_{92}	76	96
$Pd_{10}Au_{90}$	434	95
$Pd_{13}Au_{87}$	443	82
Pd_{100}	276	47
Au_{100}	0	

^{a}Based on total Pd content as determined by ICP-MS.

Figure 3. Catalytic activity and selectivity of Pd_xAu_y/RCT-SiO$_2$ in benzaldehyde hydrogenation. (a) Total conversion of benzaldehyde (green triangles) with corresponding product selectivity (bars) over Pd_xAu_y/RCT-SiO$_2$ catalysts. (b) Space−time yield (STY, red circles, based on total Pd content as determined by ICP-MS) and benzyl alcohol selectivity (blue squares) as a function of Pd content (Table 1), indicating high performance for a Pd concentration of 10−13 atom %. Reaction conditions: T_{bed} = 323 K, p = 5 bar, $F(H_2)$ = 50 mL STP min^{-1}, $F(BA)$ = 0.05 mL min^{-1}, W_{cat} = 40 mg.
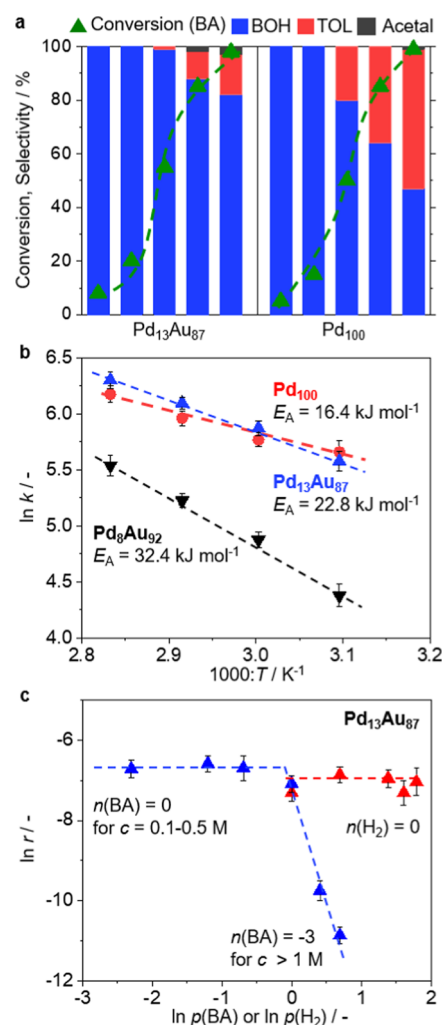

Figure 4. Reaction kinetics of benzaldehyde hydrogenation. (a) Product selectivity at different conversion levels of benzaldehyde hydrogenation over $Pd_{13}Au_{87}$ and Pd_{100}. (b) Arrhenius plots for the reaction rate constants, k, used to derive the apparent activation energy, E_A, of the Pd_8Au_{92} (black), $Pd_{13}Au_{87}$ (blue) and Pd_{100} (red) catalysts. (c) Reaction rates, r, for benzaldehyde hydrogenation on $Pd_{13}Au_{87}$ as a function of the inlet partial pressure of H$_2$ (red) or benzaldehyde (blue) concentration. Notably, the apparent partial reaction order for benzaldehyde changes from 0 to −3, depending on the concentration range (c). Reaction conditions: T_{bed} = 323 K (a, c), 323−353 K (b), p = 5 bar (a, b), 1−6 bar (c), $F(H_2)$ = 50 mL STP min^{-1}, $F(BA)$ = 0.05 mL min^{-1}, $c(BA)$ = 0.5 M (a, b), 0.1−2 M (c) in isopropanol, W_{cat} = 5−40 mg (a), W_{cat} = 10 mg (b, c). Note that the catalyst loading in (a) was adjusted for $Pd_{13}Au_{87}$ and Pd_{100} to achieve the range of conversions while keeping otherwise identical reaction conditions.

stability at elevated temperatures in oxidative[31,32] and reductive reaction atmospheres.[6,7] The latter has been ascribed to a partial embedding of the nanoparticles in the host matrix.[14] In this study, silica was chosen as the preferred
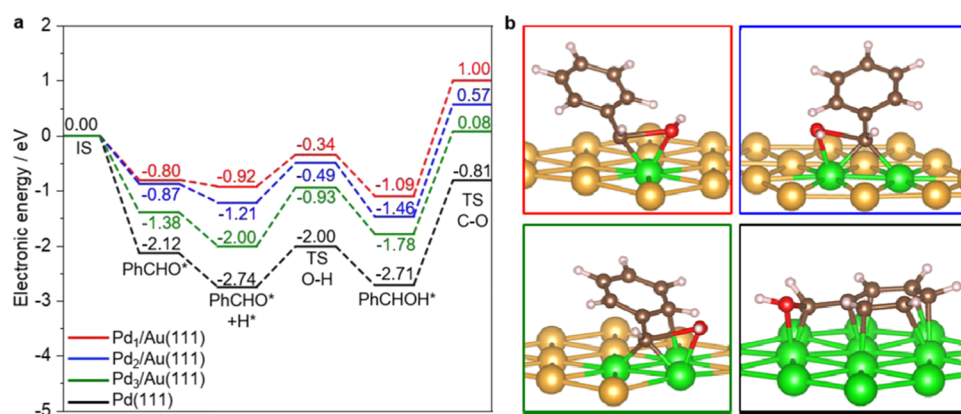
Figure 5. Benzaldehyde partial hydrogenation and deoxygenation through the PhCHOH* intermediate over Pd$_1$/Au(111) (red), Pd$_2$/Au(111) (blue), Pd$_3$/Au(111) (green), and Pd(111) (black). (a) Electronic energy pathways of partial hydrogenation of benzaldehyde (PhCHO) to PhCHOH* and subsequent deoxygenation. Increasing the size of the Pd ensemble stabilizes the PhCHOH* intermediate and slightly lowers the subsequent C−O cleavage barrier. (b) PhCHOH* C−O cleavage transition state geometries over Pd$_{1-3}$/Au(111) and Pd(111). Key: (atom: color) Au: yellow; Pd: green; C: brown; O: red; H: white.
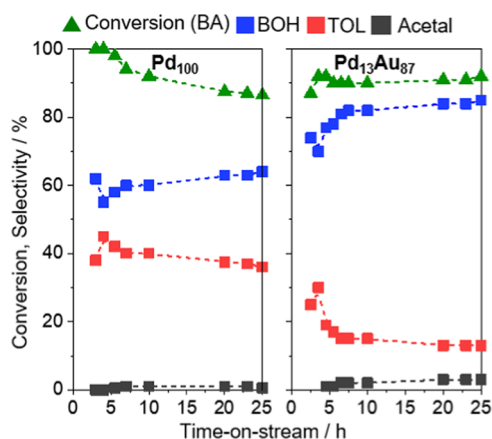

Figure 6. Time-on-stream performance in benzaldehyde hydrogenation. Stability tests of the Pd$_{100}$ and Pd$_{13}$Au$_{87}$ catalysts, showing the superior performance of the latter. Reaction conditions: T_{bed} = 323 K, p = 5 bar, $F(H_2)$ = 50 mL STP min^{-1}, $F(BA)$ = 0.05 mL min^{-1}, W_{cat} = 40 mg.

support material due to its relatively inert and nonreducible character in hydrogenation reactions.[6]

The average metal particle sizes of 7−8 nm and total metal loadings of 2.6−2.8 wt % were confirmed by transmission electron microscopy (TEM) and inductively coupled plasma mass spectrometry (ICP-MS) analysis, respectively (Figure 1a and Table 1). Scanning electron microscopy (SEM) shows an average pore diameter of 220 nm of the silica support across the RCT catalyst series (Figure 1b and S1). The Pd content in the bimetallic catalysts was varied in the range of 4, 8, 10, and 13 atom %; actual average measured compositions are shown in Table 1. Accordingly, the as-prepared catalysts are referred to as Pd$_4$Au$_{96}$, Pd$_8$Au$_{92}$, Pd$_{10}$Au$_{90}$, and Pd$_{13}$Au$_{87}$. Monometallic catalysts, Pd$_{100}$ and Au$_{100}$, as well as metal-free SiO$_2$-RCT, were also prepared as reference materials.

Previous literature shows that Pd and Au are homogeneously mixed in the as-prepared bimetallic catalysts,[6] as was corroborated by the energy-dispersive X-ray spectroscopy (EDX) intensity maps of Pd$_{13}$Au$_{87}$ (Figure S2). Note that EDX can only be used to visualize the overall metal distribution in the PdAu NPs but is not sensitive enough to detect small compositional changes in the surface layer. Partial

Pd surface enrichment upon oxygen pretreatment has therefore previously been demonstrated using X-ray absorption spectroscopy,[10,33,34] density functional theory (DFT) calculations,[10] temporal analysis of products reactor studies,[18] and catalytic testing.[10,33] X-ray photoelectron spectroscopy (XPS) analysis of the Au 4f region of the calcined catalyst (Figure 1c) indicates a predominantly zero oxidation state of Au (metallic Au; binding energy, B.E. = 84.0 ± 0.1 eV, full width at half-maximum, FWHM = 2.0)[35] with minor Au^{3+} contributions (B.E. = 86.5 ± 0.1 eV, FWHM = 2.0),[35] possibly originating from oxygen spillover from Pd onto Au during calcination.[5] Analysis of the Pd 3d region (Figure 1d) in the bimetallic catalysts is limited by the comparably small Pd content compared to that of the major component, Au, and the overlap with the Au 3d features. Deconvolution of the spectra suggests a predominantly metallic nature of Pd atoms (B.E. = 345.0 ± 0.1 eV, FWHM = 1.5),[5] with a smaller contribution of surface-oxidized sites (B.E. = 336.9 ± 0.1 eV, FWHM = 1.5). In line with previous X-ray absorption analysis of Pd-in-Au alloy catalysts,[13,31] monometallic Pd$_{100}$ was found to exhibit a larger fraction of oxidized Pd species after calcination compared to the PdAu alloys.[5]

To gain further insights into the surface composition and surface distribution of Pd in the alloy catalyst series, a recently developed method based on titrating the active species with precise pulses of O$_2$, followed by CO, from a pulse flow reactor was employed.[18] Specifically, the method builds on the high activity of preoxidized PdAu alloys in CO oxidation. By pulsing calibrated amounts of CO over the oxygen-pretreated Pd$_8$Au$_{92}$, Pd$_{10}$Au$_{90}$, and Pd$_{13}$Au$_{78}$ catalysts, CO$_2$ is formed, which is quantified using mass spectrometry. The number of CO$_2$ molecules is related to the amount of surface oxygen species, which in turn relates to the Pd content (see the Experimental Section and Supporting Information for details). Following this method, surface Pd contents of 1.12 ± 0.67, 6.78 ± 1.36, and 12.65 ± 1.41% were calculated for Pd$_8$Au$_{92}$, Pd$_{10}$Au$_{90}$, and Pd$_{13}$Au$_{78}$, respectively, assuming a degree of nanoparticle embedding in the support of 85% in the RCT catalysts[14] (Figure 2). Note that this method only counts the contiguous Pd atoms and neglects the isolated Pd single atoms since isolated Pd is unable to dissociate molecular oxygen.[36,37] Assuming a homogeneous Pd distribution within the PdAu alloy nanoparticles, the substantially lower surface Pd contents
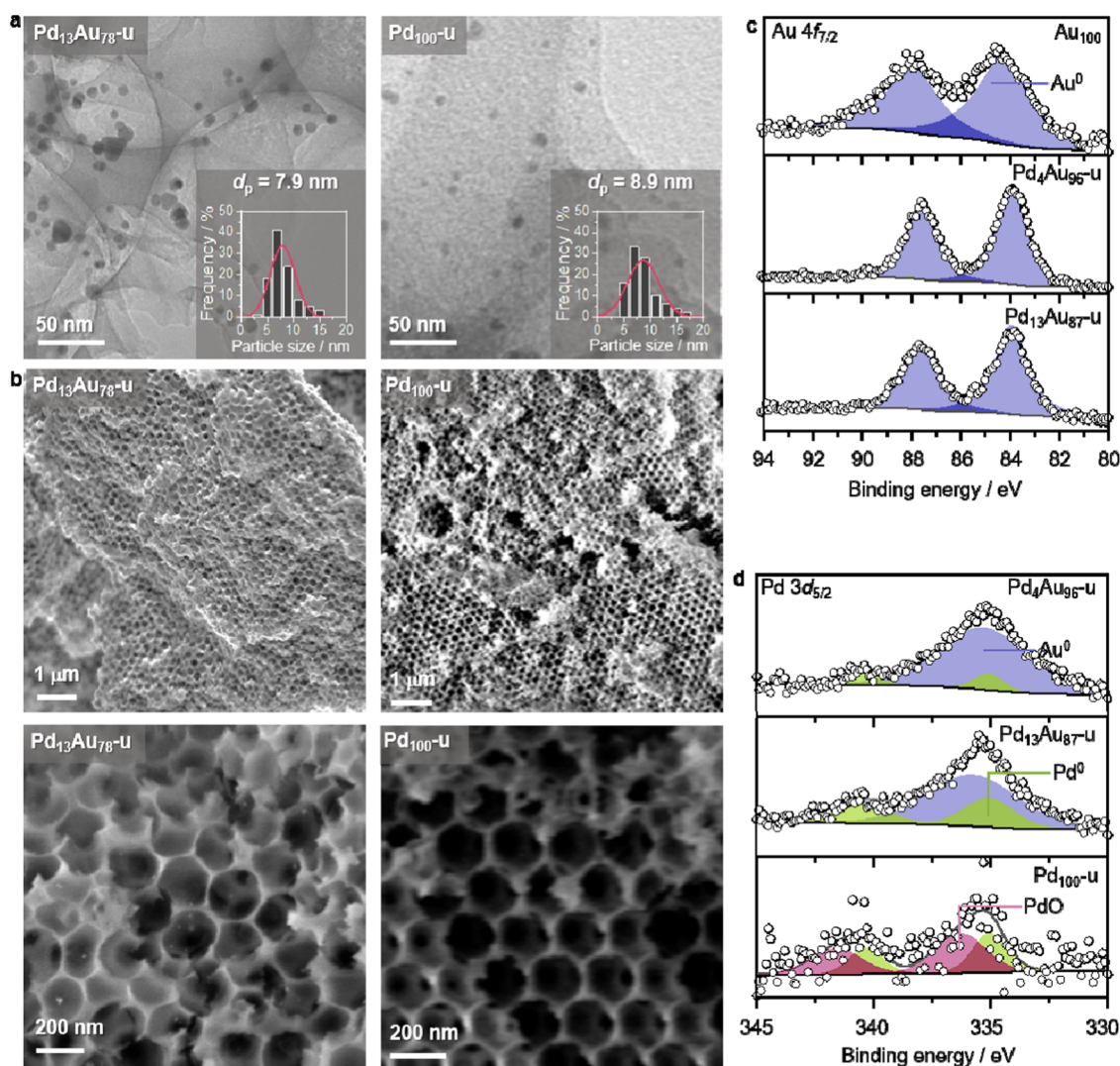
Figure 7. Characterizations of selected catalysts after use in benzaldehyde hydrogenation for 25 h, indicated by "-u" in the sample code. (a) TEM images of $Pd_{13}Au_{78}$-u and Pd_{100}-u with corresponding particle size distributions, indicating minor particle agglomeration upon exposure to the reaction atmosphere by comparison to their as-prepared analogues (Figure 1a). (b) SEM images showing the preserved macroporous structure of the support after catalysis. (c, d) XPS of the Au 4f and Pd 3d regions, indicating increasingly reduced metal sites after catalysis in comparison to the as-prepared states (Figure 1c,d).

of Pd_8Au_{92} and $Pd_{10}Au_{90}$ in the titration experiments (dashed red line in Figure 2), compared to the expected Pd contents (dashed black line in Figure 2, based on ICP-MS results), suggest the predominant and non-negligible presence of Pd single atoms in these samples, respectively. On the contrary, the surface Pd content in $Pd_{13}Au_{78}$ is in line with the expected bulk value and thus indicates the presence of mainly Pd ensembles (*e.g.*, dimers, trimers, small clusters).

Activity and Selectivity of Pd_xAu_y/RCT-SiO$_2$ in Benzaldehyde Hydrogenation. Prior to the catalytic tests, the samples were activated by exposure to a 20% O$_2$ in an Ar mixture at 773 K.[10] Subsequent to such activation, hydrogenation runs were conducted in a liquid flow reactor at a bed temperature of T_{bed} = 323 K and a pressure of p = 5 bar with a hydrogen flow of $F(H_2)$ = 50 mL STP min^{-1}. The rates and selectivity of benzaldehyde hydrogenation strongly depend on the choice of solvent.[15,38,39] Specifically, protic solvents, such as alcohols, were recently identified as suitable candidates due to their ability to coordinate and solvate sorbed hydrogen on palladium surfaces, converting them into interfacial protons,

which have been shown to promote C=O bond hydrogenation of carbonyl groups.[15,40] Among the protic solvents, we herein selected isopropanol as the solvent for the added benefit of its environmentally benign and non-hazardous characteristics in combination with a relatively lower propensity to form acetals as compared to other alcohols with less steric demands. *o*-Xylene was chosen as an internal standard and verified to not affect the rate or selectivity in benzaldehyde hydrogenation (Figure S3).

Benzaldehyde (0.5 M) and *o*-xylene (0.2 M) dissolved in isopropanol were fed over the catalyst (weight, W_{cat} = 40 mg) at a flow of 0.05 mL min^{-1}. Product analysis at the reactor outlet was carried out using *ex situ* gas chromatography coupled to mass spectrometry (GC-MS). Steady state was reached in approx. 60 min, following previous flow equilibration for additional 60 min, during which the catalyst was exposed to the reducing atmosphere for a total of 120 min. Typically, the hydrogenation of benzaldehyde (BA) yielded benzyl alcohol (BOH) as the primary hydrogenation product with toluene (TOL) as a secondary product (Figure 3a). The

Au_{100} and metal-free SiO_2-RCT catalysts were found to be inherently inactive under these reaction conditions.

Benzaldehyde conversion markedly increased with increasing Pd content of the RCT catalysts (Figure 3a). Notably, Pd_4Au_{96} and Pd_8Au_{92} displayed only marginal hydrogenation activity, exhibiting conversions of only 2 and 4%, respectively. A steep increase in activity was found over the $Pd_{10}Au_{90}$ and $Pd_{13}Au_{87}$ catalysts, which showed benzaldehyde conversions of 60 and 97%, respectively, with the latter comparable to Pd_{100} (98%). However, the catalysts that exhibited the highest conversions also showed decreased selectivity to benzyl alcohol due to the formation of toluene. Besides benzyl alcohol, toluene, and trace amounts of acetal, presumably resulting from the reaction of benzaldehyde with isopropanol,[41] no additional products were detected by GC-MS analysis. No detectable hydrogenation of the aromatic ring was observed under the selected reaction conditions. While the fraction of toluene was found to be <5% for the catalysts with a Pd concentration below 10 atom %, the $Pd_{13}Au_{87}$ and Pd_{100} catalysts displayed a toluene selectivity of 15 and 43%, respectively, at conversion levels of 98%. Consequently, space−time yields (STYs, based on total Pd content as determined by ICP-MS) of benzyl alcohol (Figure 3b) were maximized over the $Pd_{10}Au_{90}$ and $Pd_{13}Au_{87}$ catalysts, outperforming monometallic Pd_{100} by 1.5 fold (Table 2).

To ensure that the activity hierarchy of the Pd_xAu_y/RCT-SiO_2 series is intrinsic to benzaldehyde hydrogenation and not dependent on the chosen reactor mode, we reproduced key experiments in batch mode (Figure S4). Benzaldehyde conversion (X_{BA}) and the corresponding first-order kinetic plots (with first-order rate constant k) as a function of reaction time are in good agreement with the activity trends obtained in the flow experiments.

To test the effect of benzaldehyde conversion on product selectivity, the loading of both $Pd_{13}Au_{87}$ and Pd_{100} ($W_{cat} = 5-40$ mg) was adjusted to achieve similar conversions from 10 to 100% under identical reaction conditions. At conversion levels below 20%, both catalysts exclusively produce benzyl alcohol (Figure 4a). With larger catalyst loadings, and thus higher benzaldehyde conversion, toluene formation became more prevalent. However, Pd_{100} produced considerably more toluene compared to $Pd_{13}Au_{87}$ over the entire range of conversion. To test whether toluene was formed from the reaction of benzyl alcohol, benzyl alcohol was co-fed in the reactant mixture (Figure S5). At benzaldehyde conversion levels of 20%, co-feeding of 0.5 M benzyl alcohol (to the reaction feed of 0.5 M benzaldehyde) did not alter the benzaldehyde conversion level or the product selectivity. Thus, the benzyl alcohol does not appear to inhibit the reaction or lead to the formation of toluene. Indeed, feeding 0.5 M benzyl alcohol alone (without benzaldehyde) produced no conversion; the direct sequential formation of toluene from benzyl alcohol under the selected reaction conditions can be excluded.

Kinetic studies of $Pd_{13}Au_{87}$ and Pd_{100} were performed in order to compare these catalysts to previous studies of monometallic Pd-based catalysts (Figure 4b). In the temperature range between 323−523 K, an apparent activation energy, E_A, of 16.4 kJ mol^{-1} was found for Pd_{100}, in agreement with previous studies.[42] $Pd_{13}Au_{87}$ also exhibited a comparably low apparent activation energy of 22.8 kJ mol^{-1}, whereas, in contrast, Pd_8Au_{92} showed a significantly higher value of 32.4 kJ mol^{-1}. These results emphasize the closer resemblance of the hydrogenation activity of $Pd_{13}Au_{87}$ to monometallic palladium

than to the more dilute PdAu alloys. The partial reaction order of hydrogen in the pressure range of 1−6 bar was found to be 0 over $Pd_{13}Au_{87}$, indicative of H saturation of the available sites (Figure 4c). Notably, these results are distinctly different from the order of 1, found under typical conditions for previous studies of Pd catalysts in batch mode and likely originate from the significant excess of hydrogen (H_2/BA ratio ≥100 times) in the here applied reaction conditions in flow mode.[15,42] On the other hand, the reaction order of benzaldehyde was found to be 0 in the concentration range between 0.1 and 1 M in agreement with the previous batch studies. Above this range, the reaction was inhibited by benzaldehyde, ultimately leading to catalyst deactivation at higher concentrations.

To assess the importance of substrate aromaticity on the reactivity of the aldehyde, the hydrogenation of cyclohexanecarboxaldehyde, the fully saturated structural analogue of benzaldehyde was attempted over $Pd_{13}Au_{87}$ and Pd_{100} (Figure S6). Under identical reaction conditions of benzaldehyde hydrogenation, no conversion was detectable. Even upon increasing the temperature to $T_{bed} = 423$ K and the H_2 pressure to $p = 8$ bar, neither catalyst showed any activity for this reaction, indicating the key role of the aromatic ring in facilitating aldehyde hydrogenation. These observations are fully in line with previous literature, studying the effect of the side chains of aldehydes for hydrogenation reactivity over Pd-based catalysts. Therein, the authors did not observe any conversion of cyclohexanecarboxaldehyde and other saturated aldehydes as well and identified strong π-electron conjugation as the prerequisite for electronic activation of the carbonyl group.[43]

Mechanistic Theoretical Considerations on the Ensemble Size Effect. To rationalize the experimentally observed activity and selectivity trends, density functional theory (DFT) calculations were performed to investigate the effect of the Pd ensemble size on the energetics of the adsorption and hydrogenation of benzaldehyde (PhCHO, Ph as the phenyl group) and on the deoxygenation of partially hydrogenated PhCHO. Following our previous investigation of the H_2/D_2 exchange reaction over dilute Pd-in-Au catalysts, we simulated the Pd active sites of the dilute Pd-in-Au catalysts by replacing Au atoms on the Au(111) surface with Pd.[6] Such Pd_{1-3} surface ensembles were found to be adequate in describing the H_2/D_2 exchange kinetics over dilute Pd-in-Au catalysts.[33] Overall, it was found that increasing the Pd ensemble size from Pd_1 to Pd_3 strengthens the adsorption of intermediates and reduces the C−O bond cleavage barrier of partially hydrogenated intermediates. The adsorption of PhCHO progressively strengthens as the Pd ensemble size increases from single atoms (Pd_1, representing Pd_4Au_{96}/SiO_2-RCT) to dimers (Pd_2) and trimers (Pd_3, representing $Pd_{13}Au_{87}$/SiO_2-RCT Figure 5), and finally to bulk palladium (Pd(111), representing Pd_{100}/SiO_2-RCT). Specifically, it becomes more negative (stable) from −0.80 eV over Pd_1 to −2.12 eV over Pd(111) (Table S1). The same trend is observed for the stability of the transition state (TS) of the O−H bond formation step to PhCHOH* (star indicates an adsorbed species on the catalyst surface), where, from Pd_1 to Pd(111), the energy of the O−H bond formation TS (relative to gas phase PhCHO and H_2) is stabilized from −0.34 to −2.00 eV. Although it could appear that Pd_4Au_{96}/SiO_2-RCT might be the most active (as the C−H bond formation barrier is the lowest over Pd_1), it should be noted that the adsorption of PhCHO on all sites would require a loss in liquid-phase

entropy, which, in turn, would increase the free energy of the subsequent TS. As PhCHO is least strongly bound on both Pd_1 and Pd_2, the loss of entropy would harm the reactivity of those sites the most. Continuing in the reaction pathway, the PhCHOH* product of the hydrogenation step shows the same trend in stability with the Pd ensemble size as PhCHO, as its adsorption energy is also strengthened by increasingly larger Pd ensembles. Since the C radical of the PhCHOH* intermediate is a part of the conjugated system, a progressively larger fraction of the aromatic ring can adsorb on Pd_{1-3}. For all Pd structures considered, the PhCHOH* intermediate was found to be more stable than the $PhCH_2O^*$ intermediate (Figure S7), making it likely for the benzaldehyde hydrogenation reaction to mainly take place through PhCHOH* over Pd ensembles on Au(111). Finally, for the TS of the PhCH−OH bond cleavage, a smaller impact of ensemble size is observed on the barrier, where the deoxygenation barrier only decreases from 2.09 to 1.90 eV moving from $Pd_1Au(111)$ to Pd(111) (Table S1). To compare the selectivity of Pd-in-Au catalysts and Pd for benzaldehyde hydrogenation and deoxygenation, the full energy profiles of the reactions over $Pd_3/Au(111)$ and Pd(111) through the PhCHOH* intermediate were calculated (Figure S8). For both $Pd_3/Au(111)$ and Pd(111), the hydrogenation barrier to form benzyl alcohol was found to be lower than deoxygenation, resulting in higher selectivity for benzyl alcohol over toluene.

For comparison, the impact of the Pd ensemble size on the hydrogenation of benzaldehyde to $PhCH_2O^*$ and its subsequent deoxygenation was also examined (Figure S8). As for PhCHOH*, the same trend in stability was observed for the TS of the C−H bond formation step to $PhCH_2O^*$. Next, in contrast to the PhCHOH* intermediate, adsorption by only the O radical was found to be the most stable configuration of $PhCH_2O^*$ on the Pd_1−Pd_3 ensembles, while adsorption of the full aromatic ring was found to be possible on Pd(111). The changing $PhCH_2O^*$ adsorption configuration from the small Pd ensembles to Pd(111) impacts the geometry of the TS of $PhCH_2$−O* bond cleavage. For Pd_1−Pd_3, the aromatic ring is lifted off the surface, while the ring can still contact with Pd(111). The contact between the aromatic ring and the Pd(111) surface stabilizes the TS, lowering the C−O bond cleavage barrier from 1.62 eV over Pd_1 to 1.16 eV over Pd(111), implying that there is a higher chance for the C−O bond of the $PhCH_2O^*$ intermediate to be cleaved over large Pd ensembles resembling Pd(111) (Table S1).

It is most likely that an optimum in conversion and selectivity originates from a compromise between the adsorption strength of PhCHO hydrogenation intermediates and the C−C bond cleavage barrier due to the active site ensemble size. On Pd_1, only the oxygen of the aldehyde group can adsorb on the Pd site. The resulting η^1 configuration is weakly bound to Pd_1, with an adsorption energy of −0.80 eV (Figure S9). On Pd_2, the aromatic ring can now partially adsorb on the Pd ensemble, oriented at the bridge site between the two Pd atoms. This adsorption geometry is reminiscent of the "bri30" adsorption configuration of benzene, where the π-conjugated system makes a 30° angle with the close-packed direction.[44] Compared to Pd_1, the adsorption energy is slightly strengthened to −0.87 eV. Increasing the ensemble size to Pd_3, the aromatic ring can fully adsorb on the surface. Here, the aromatic ring is situated at the face-centered cubic (FCC) site at the center of the Pd_3 ensemble, reminiscent of the "FCC0" configuration of benzene. Compared to Pd_1 and Pd_2, the

adsorption energy of PhCHO is much stronger on Pd_3 at −1.38 eV. Here, by comparing the adsorption configuration and strength of cyclohexanecarboxaldehyde ($C_6H_{11}CHO$) with that of PhCHO on Pd_3, the importance of the π-conjugated system in stabilizing reaction intermediates is apparent. Different from PhCHO, $C_6H_{11}CHO$ adsorbs on Pd_3 in an η^1 configuration through only the oxygen of the aldehyde group; as such, its adsorption strength is much weaker at −0.98 eV. (Figure S9e) As an alternative to the geometric effect, we also examined the possibility of electronic effects on the adsorption. The trend of PhCHO adsorption energy is not correlated to electronic effects, as the center of the Pd 4d states does not change significantly with increasing ensemble size: the Pd 4d state center is essentially identical from Pd_1 to Pd_3 (Figure S10).

As further confirmation of the geometric effect, the adsorption energy of PhCHO on contiguous Pd surfaces was also compared (Figure S11). Three such surfaces were compared: Pd(111), a Pd monolayer (Pd_{ML}) atop Au(111), and $Pd_{ML}/Au(111)$ under compressive strain, where the lattice spacing of the Au substrate was set to that of bulk Pd. On all three surfaces, PhCHO prefers to adsorb in the "bri30" configuration, hence limiting variations in adsorption energy to mainly electronic contributions. The adsorption energy is the weakest on $Pd_{ML}/Au(111)$ under strain at −2.09 eV, while it is the strongest on $Pd_{ML}/Au(111)$ under no strain at −2.31 eV (Figure S12). For reference, on Pd(111), the adsorption energy of PhCHO is close to that of $Pd_{ML}/Au(111)$ under compressive strain at −2.12 eV. From Pd(111) and $Pd_{ML}/Au(111)$ under compressive strain to $Pd_{ML}/Au(111)$ under no strain, the Pd 4d band center rises from −1.81 and −1.75 to −1.48 eV relative to the Fermi energy of each respective surface. Although an upshift in the Pd 4d band center noticeably strengthens the adsorption energy of PhCHO, the shift is much smaller than that among Pd ensembles of increasing size. As such, the geometry of the active ensemble size is the main contributor to variations in adsorption energy.

Catalyst Stability and Deactivation. The stability of the most active alloy, $Pd_{13}Au_{87}$, was compared to that of monometallic Pd_{100} for benzaldehyde hydrogenation with 25 h time-on-stream tests at 323 K and 5 bar (Figure 6). Full conversion levels were initially observed for Pd_{100}, but it deactivated to 86% over 25 h. On the contrary, $Pd_{13}Au_{87}$ maintained a stable conversion of 93% at comparable benzyl alcohol selectivity (85−87%) for 20 h after an initial equilibration period. The higher stability of $Pd_{13}Au_{87}$ compared to Pd_{100} was further confirmed at lower conversion levels (<20%) and, thus, in the absence of toluene formation (Figure S13).

To rationalize the diverging stability trends between the monometallic Pd_{100} and the bimetallic $Pd_{13}Au_{87}$ catalysts, both were examined *ex situ* after being subjected to the reaction conditions. Accordingly, the used samples were retrieved after the 25 h tests (sample code -u) for characterization by TEM, SEM, EDX, XPS, ICP-MS, and temperature-programmed oxidation (TPO). TEM showed a slight increase in the average metal particle size for $Pd_{13}Au_{87}$ from 6.7 nm in the as-prepared (Figure 1a) to 7.9 nm in the used catalyst (Figure 7a). A more significant increment in the average metal particle size was found for Pd_{100} (6.8 to 8.9 nm), suggesting particle agglomeration as a possible deactivation path. Notably, the tendency to agglomerate was lower in the $Pd_{13}Au_{87}$ catalyst in line with their respective catalytic performance.

Comparison of the as-prepared and used Pd_{100} and $Pd_{13}Au_{87}$ catalysts by SEM (Figures 1b and 7b) indicates that the ordered pore structure of the silica support was preserved in both cases, indicating structural stability and thus the applicability of RCT-based catalysts for liquid-phase hydrogenations with pressures up to 5 bar. ICP-MS analysis of the used Pd_{100} and $Pd_{13}Au_{87}$ catalysts confirmed preservation of the metal loading in both cases, excluding metal leaching as deactivation path. Specifically, the metal content of Pd_{100} and $Pd_{13}Au_{87}$ remained at 0.4 and 2.7 wt % with a Pd content of 14 atom % in the latter case (compared to 13.5 atom % in the as-prepared sample, Table 1). In line with the preserved metal contents, the metal distribution also remained comparable in the used $Pd_{13}Au_{87}$ and as-prepared sample catalysts, though due to sample drift during the measurement, the results are not definitive in Figure S2b.

XPS analysis of the used $Pd_{13}Au_{87}$ and Pd_4Au_{96} catalysts showed an increased fraction of reduced/metallic Au in the Au 4f spectra (Figure 7c), compared to the as-prepared samples (Figure 1e), suggesting that Au is fully reduced under the reductive atmosphere during benzaldehyde hydrogenation. Similarly, inspection of the Pd 3d region also indicates that the Pd sites are increasingly reduced after exposure to the reaction conditions in all catalysts (Figure 7d). Comparison of the C 1s spectra of the as-prepared and used catalysts shows no apparent changes, suggesting the absence of coke deposits (Figure S14).

To further confirm this, TPO was conducted in a diluted oxygen atmosphere (Figure S15). No O_2 consumption ($m/z = 32$) or CO_2 formation ($m/z = 44$) was detected over the investigated temperature range on both Pd_{100} and $Pd_{13}Au_{87}$ catalysts after benzaldehyde hydrogenation for 25 h time-on-stream, corroborating the absence of carbonaceous deposits. This result is in line with the unchanged optical appearance and color of the used catalysts and excludes coke formation as a relevant deactivation path.

CONCLUSIONS

The reaction kinetics and selectivity for benzaldehyde hydrogenation on dilute Pd-in-Au nanoparticle RCT catalysts are controlled by the size of surface Pd ensembles. While Pd single atoms (4 atom % Pd in Au) are virtually inactive, benzyl alcohol production is the highest over small Pd clusters expected to form between 10−12 atom % Pd in Au. The activity trend likely originates from the fact that the precursor state of benzaldehyde hydrogenation is too weakly bound on Pd single atoms and both the adsorption of benzaldehyde and the stabilization of the transition state of the C−H bond formation step progressively strengthen with the number of Pd atoms. Further increasing the Pd ensemble size above 10−12 atom % Pd in Au leads to the onset of hydrogenolysis, promoting toluene formation, in line with a relatively lowered C−O bond cleavage barrier. The nanostructured $Pd_{13}Au_{87}/SiO_2$-RCT catalyst is however much more selective for hydrogenation compared to pure Pd RCT catalysts (82 *vs* 47%) at comparable conversion (~98%) and activity (~500 $mmol_{Benzaldehyde}$ s^{-1} mol_{Pd}^{-1}). Remarkably, the catalyst stability is also improved in the $Pd_{13}Au_{87}/SiO_2$-RCT due to inhibited particle agglomeration.

ASSOCIATED CONTENT

Ⓢ Supporting Information

The Supporting Information is available free of charge at https://pubs.acs.org/doi/10.1021/acscatal.3c02671.

Details on the method for estimating the number of surface atoms by O_2 titration; additional characterization data (SEM, EDX, XPS, TPO), catalytic data from flow and batch reactors, and DFT calculations (PDF)

Optimized geometries of structural models used in DFT calculations (ZIP)

AUTHOR INFORMATION

Corresponding Authors

Philippe Sautet − *Department of Chemical and Biomolecular Engineering, University of California, Los Angeles, California 90095, United States; Department of Chemistry and Biochemistry, University of California, Los Angeles, California 90095, United States;* Ⓞ orcid.org/0000-0002-8444-3348; Email: sautet@ucla.edu

Cynthia M. Friend − *Department of Chemistry and Chemical Biology, Harvard University, Cambridge, Massachusetts 02138, United States; John A. Paulson School of Engineering and Applied Sciences, Harvard University, Cambridge, Massachusetts 02138, United States;* Ⓞ orcid.org/0000-0002-8673-9046; Email: friend@fas.harvard.edu

$^\nabla$**Robert J. Madix** − *Department of Chemistry and Chemical Biology, Harvard University, Cambridge, Massachusetts 02138, United States; John A. Paulson School of Engineering and Applied Sciences, Harvard University, Cambridge, Massachusetts 02138, United States;* Ⓞ orcid.org/0000-0002-3132-2382; Email: rmadix@seas.harvard.edu

Authors

Selina K. Kaiser − *Department of Chemistry and Chemical Biology, Harvard University, Cambridge, Massachusetts 02138, United States; John A. Paulson School of Engineering and Applied Sciences, Harvard University, Cambridge, Massachusetts 02138, United States*

Jessi E. S. van der Hoeven − *Department of Chemistry and Chemical Biology, Harvard University, Cambridge, Massachusetts 02138, United States; John A. Paulson School of Engineering and Applied Sciences, Harvard University, Cambridge, Massachusetts 02138, United States; Materials Chemistry and Catalysis, Debye Institute for Nanomaterials Science, Utrecht University, 3584 CG Utrecht, The Netherlands;* Ⓞ orcid.org/0000-0001-9832-289X

George Yan − *Department of Chemical and Biomolecular Engineering, University of California, Los Angeles, California 90095, United States*

Kang Rui Garrick Lim − *Department of Chemistry and Chemical Biology, Harvard University, Cambridge, Massachusetts 02138, United States;* Ⓞ orcid.org/0000-0003-2159-9844

Hio Tong Ngan − *Department of Chemical and Biomolecular Engineering, University of California, Los Angeles, California 90095, United States*

Sadhya Garg − *John A. Paulson School of Engineering and Applied Sciences, Harvard University, Cambridge, Massachusetts 02138, United States*

Mustafa Karatok − *Department of Chemistry and Chemical Biology, Harvard University, Cambridge, Massachusetts 02138, United States; Department of Nanotechnology and*

Nanomedicine, Hacettepe University, 06800 Ankara, Türkiye; ⊙ orcid.org/0000-0001-5509-5463

Michael Aizenberg − *John A. Paulson School of Engineering and Applied Sciences, Harvard University, Cambridge, Massachusetts 02138, United States;* ⊙ orcid.org/0000-0002-2901-7012

Joanna Aizenberg − *Department of Chemistry and Chemical Biology, Harvard University, Cambridge, Massachusetts 02138, United States; John A. Paulson School of Engineering and Applied Sciences, Harvard University, Cambridge, Massachusetts 02138, United States;* ⊙ orcid.org/0000-0002-2343-8705

Complete contact information is available at:
https://pubs.acs.org/10.1021/acscatal.3c02671

Notes

◼ REFERENCES

(1) Hagen, J. *Industrial Catalysis: A Practical Approach*; Wiley-VCH Verlag, 2015.

(2) Kyriakou, G.; Boucher, M. B.; Jewell, A. D.; Lewis, E. A.; Lawton, T. J.; Baber, A. E.; Tierney, H. L.; Flytzani-Stephanopoulos, M.; Sykes, E. C. Isolated Metal Atom Geometries as a Strategy for Selective Heterogeneous Hydrogenations. *Science* **2012**, *335*, 1209−1212.

(3) Zhang, L.; Zhou, M.; Wang, A.; Zhang, T. Selective Hydrogenation over Supported Metal Catalysts: From Nanoparticles to Single Atoms. *Chem. Rev.* **2020**, *120*, 683−733.

(4) Hannagan, R. T.; Giannakakis, G.; Flytzani-Stephanopoulos, M.; Sykes, E. C. H. Single-Atom Alloy Catalysis. *Chem. Rev.* **2020**, *120*, 12044−12088.

(5) Kaiser, S. K.; Chen, Z.; Faust Akl, D.; Mitchell, S.; Pérez-Ramírez, J. Single-Atom Catalysts across the Periodic Table. *Chem. Rev.* **2020**, *120*, 11703−11809.

(6) van der Hoeven, J. E. S.; Ngan, H. T.; Taylor, A.; Eagan, N. M.; Aizenberg, J.; Sautet, P.; Madix, R. J.; Friend, C. M. Entropic Control of Hd Exchange Rates over Dilute Pd-in-Au Alloy Nanoparticle Catalysts. *ACS Catal.* **2021**, *11*, 6971−6981.

(7) Luneau, M.; Shirman, T.; Foucher, A. C.; Duanmu, K.; Verbart, D. M. A.; Sautet, P.; Stach, E. A.; Aizenberg, J.; Madix, R. J.; Friend, C. M. Achieving High Selectivity for Alkyne Hydrogenation at High Conversions with Compositionally Optimized Pdau Nanoparticle Catalysts in Raspberry Colloid-Templated Sio₂. *ACS Catal.* **2020**, *10*, 441−450.

(8) Boucher, M. B.; Zugic, B.; Cladaras, G.; Kammert, J.; Marcinkowski, M. D.; Lawton, T. J.; Sykes, E. C.; Flytzani-Stephanopoulos, M. Single Atom Alloy Surface Analogs in $Pd_{0.18}cu_{15}$ Nanoparticles for Selective Hydrogenation Reactions. *Phys. Chem. Chem. Phys.* **2013**, *15*, 12187−12196.

(9) Liu, J.; Uhlman, M. B.; Montemore, M. M.; Trimpalis, A.; Giannakakis, G.; Shan, J.; Cao, S.; Hannagan, R. T.; Sykes, E. C. H.; Flytzani-Stephanopoulos, M. Integrated Catalysis-Surface Science-Theory Approach to Understand Selectivity in the Hydrogenation of 1-Hexyne to 1-Hexene on Pdau Single-Atom Alloy Catalysts. *ACS Catal.* **2019**, *9*, 8757−8765.

(10) Luneau, M.; Guan, E.; Chen, W.; Foucher, A. C.; Marcella, N.; Shirman, T.; Verbart, D. M. A.; Aizenberg, J.; Aizenberg, M.; Stach, E. A.; et al. Enhancing Catalytic Performance of Dilute Metal Alloy Nanomaterials. *Commun. Chem.* **2020**, *3*, No. 46.

(11) Furukawa, S.; Komatsu, T. Selective Hydrogenation of Functionalized Alkynes to (E)-Alkenes, Using Ordered Alloys as Catalysts. *ACS Catal.* **2016**, *6*, 2121−2125.

(12) Luneau, M.; Lim, J. S.; Patel, D. A.; Sykes, E. C. H.; Friend, C. M.; Sautet, P. Guidelines to Achieving High Selectivity for the Hydrogenation of Alpha,Beta-Unsaturated Aldehydes with Bimetallic and Dilute Alloy Catalysts: A Review. *Chem. Rev.* **2020**, *120*, 12834−12872.

(13) Shirman, E.; Shirman, T.; Shneidman, A. V.; Grinthal, A.; Phillips, K. R.; Whelan, H.; Bulger, E.; Abramovitch, M.; Patil, J.; Nevarez, R.; et al. Modular Design of Advanced Catalytic Materials Using Hybrid Organic−Inorganic Raspberry Particles. *Adv. Funct. Mater.* **2017**, *28*, No. 1704559.

(14) Hoeven, J. E. S.; Krämer, S.; Dussi, S.; Shirman, T.; Park, K. C. K.; Rycroft, C. H.; Bell, D. C.; Friend, C. M.; Aizenberg, J. On the Origin of Sinter-Resistance and Catalyst Accessibility in Raspberry-Colloid-Templated Catalyst Design. *Adv. Funct. Mater.* **2021**, *31*, No. 2106876.

(15) Cheng, G.; Jentys, A.; Gutiérrez, O. Y.; Liu, Y.; Chin, Y.-H.; Lercher, J. A. Critical Role of Solvent-Modulated Hydrogen-Binding Strength in the Catalytic Hydrogenation of Benzaldehyde on Palladium. *Nat. Catal.* **2021**, *4*, 976−985.

(16) Grabar, K. C.; Allison, K. J.; Baker, B. E.; Bright, R. M.; Brown, K. R.; Freeman, R. G.; Fox, A. P.; Keating, C. D.; Musick, M. D.; Natan, M. J. Two-Dimensional Arrays of Colloidal Gold Particles: A Flexible Approach to Macroscopic Metal Surfaces. *Langmuir* **1996**, *12*, 2353−2361.

(17) Gleaves, J. T.; Yablonskii, G. S.; Phanawadee, P.; Schuurman, Y. Tap-2: An Interrogative Kinetics Approach. *Appl. Catal., A* **1997**, *160*, 55−88.

(18) Karatok, M.; Madix, R. J.; van der Hoeven, J. E. S.; Aizenberg, J.; Reece, C. Quantifying Oxygen Induced Surface Enrichment of a Dilute Pdau Alloy Catalyst. *Catal. Sci. Technol.* **2021**, *11*, 7530−7534.

(19) Kresse, G.; Furthmüller, J. Efficient Iterative Schemes for *Ab Initio* Total-Energy Calculations Using a Plane-Wave Basis Set. *Phys. Rev. B* **1996**, *54*, 11169−11186.

(20) Kresse, G.; Hafner, J. *Ab Initio* Molecular Dynamics for Liquid Metals. *Phys. Rev. B* **1993**, *47*, 558−561.

(21) Kresse, G.; Furthmüller, J. Efficiency of *Ab-Initio* Total Energy Calculations for Metals and Semiconductors Using a Plane-Wave Basis Set. *Comput. Mater. Sci.* **1996**, *6*, 15−50.

(22) Perdew, J. P.; Burke, K.; Ernzerhof, M. Generalized Gradient Approximation Made Simple. *Phys. Rev. Lett.* **1996**, *77*, 3865−3868.

(23) Blöchl, P. E. Projector Augmented-Wave Method. *Phys. Rev. B* **1994**, *50*, 17953−17979.

(24) Kresse, G.; Joubert, D. From Ultrasoft Pseudopotentials to the Projector Augmented-Wave Method. *Phys. Rev. B* **1999**, *59*, No. 1758.

(25) Steinmann, S. N.; Corminboeuf, C. A Generalized-Gradient Approximation Exchange Hole Model for Dispersion Coefficients. *J. Chem. Phys.* **2011**, *134*, No. 044117.

(26) Steinmann, S. N.; Corminboeuf, C. Comprehensive Benchmarking of a Density-Dependent Dispersion Correction. *J. Chem. Theory Comput.* **2011**, *7*, 3567−3577.

(27) Henkelman, G.; Uberuaga, B. P.; Jónsson, H. A Climbing Image Nudged Elastic Band Method for Finding Saddle Points and Minimum Energy Paths. *J. Chem. Phys.* **2000**, *113*, 9901−9904.

(28) Henkelman, G.; Jónsson, H. Improved Tangent Estimate in the Nudged Elastic Band Method for Finding Minimum Energy Paths and Saddle Points. *J. Chem. Phys.* **2000**, *113*, 9978−9985.

(29) Henkelman, G.; Jónsson, H. A Dimer Method for Finding Saddle Points on High Dimensional Potential Surfaces Using Only First Derivatives. *J. Chem. Phys.* **1999**, *111*, 7010−7022.

(30) Monkhorst, H. J.; Pack, J. D. Special Points for Brillouin-Zone Integrations. *Phys. Rev. B* **1976**, *13*, 5188−5192.

(31) Luneau, M.; Shirman, T.; Filie, A.; Timoshenko, J.; Chen, W.; Trimpalis, A.; Flytzani-Stephanopoulos, M.; Kaxiras, E.; Frenkel, A. I.; Aizenberg, J.; et al. Dilute Pd/Au Alloy Nanoparticles Embedded in Colloid-Templated Porous Sio2: Stable Au-Based Oxidation Catalysts. *Chem. Mater.* **2019**, *31*, 5759−5768.

(32) Shirman, T.; Toops, T. J.; Shirman, E.; Shneidman, A. V.; Liu, S.; Gurkin, K.; Alvarenga, J.; Lewandowski, M. P.; Aizenberg, M.; Aizenberg, J. Raspberry Colloid-Templated Approach for the Synthesis of Palladium-Based Oxidation Catalysts with Enhanced Hydrothermal Stability and Low-Temperature Activity. *Catal. Today* **2021**, *360*, 241−251.

(33) Marcella, N.; Lim, J. S.; Plonka, A. M.; Yan, G.; Owen, C. J.; van der Hoeven, J. E. S.; Foucher, A. C.; Ngan, H. T.; Torrisi, S. B.; Marinkovic, N. S.; et al. Decoding Reactive Structures in Dilute Alloy Catalysts. *Nat. Commun.* **2022**, *13*, No. 832.

(34) Marcella, N.; Liu, Y.; Timoshenko, J.; Guan, E.; Luneau, M.; Shirman, T.; Plonka, A. M.; van der Hoeven, J. E. S.; Aizenberg, J.; Friend, C. M.; Frenkel, A. I. Neural Network Assisted Analysis of Bimetallic Nanocatalysts Using X-Ray Absorption near Edge Structure Spectroscopy. *Phys. Chem. Chem. Phys.* **2020**, *22*, 18902−18910.

(35) Casaletto, M. P.; Longo, A.; Martorana, A.; Prestianni, A.; Venezia, A. M. Xps Study of Supported Gold Catalysts: The Role of Au^0 and $Au^{+\Delta}$ Species as Active Sites. *Surf. Interface Anal.* **2006**, *38*, 215−218.

(36) Gao, F.; Wang, Y.; Goodman, D. W. Co Oxidation over Aupd(100) from Ultrahigh Vacuum to near-Atmospheric Pressures: The Critical Role of Contiguous Pd Atoms. *J. Am. Chem. Soc.* **2009**, *131*, 5734−5735.

(37) Yu, W.-Y.; Zhang, L.; Mullen, G. M.; Henkelman, G.; Mullins, C. B. Oxygen Activation and Reaction on Pd−Au Bimetallic Surfaces. *J. Phys. Chem. C* **2015**, *119*, 11754−11762.

(38) Claus, P. Selective hydrogenation of α,β-unsaturated aldehydes and other C=O and C=C bonds containing compounds. *Top. Catal.* **1998**, *5*, 51−62.

(39) Bertero, N. M.; Trasarti, A. F.; Apesteguía, C. R.; Marchi, A. J. Solvent Effect in the Liquid-Phase Hydrogenation of Acetophenone over Ni/Sio2: A Comprehensive Study of the Phenomenon. *Appl. Catal., A* **2011**, *394*, 228−238.

(40) Shangguan, J.; Chin, Y.-H. C. Kinetic Significance of Proton−Electron Transfer During Condensed Phase Reduction of Carbonyls on Transition Metal Clusters. *ACS Catal.* **2019**, *9*, 1763−1778.

(41) Bhanushali, J. T.; Kainthla, I.; Keri, R. S.; Nagaraja, B. M. Catalytic Hydrogenation of Benzaldehyde for Selective Synthesis of Benzyl Alcohol: A Review. *ChemistrySelect* **2016**, *1*, 3839−3853.

(42) Divakar, D.; Manikandan, D.; Kalidoss, G.; Sivakumar, T. Hydrogenation of Benzaldehyde over Palladium Intercalated Bentonite Catalysts: Kinetic Studies. *Catal. Lett.* **2008**, *125*, 277−282.

(43) Cattaneo, S.; Capelli, S.; Stucchi, M.; Bossola, F.; Dal Santo, V.; Araujo-Lopez, E.; Sharapa, D. I.; Studt, F.; Villa, A.; Chieregato, A.; et al. Discovering the Role of Substrate in Aldehyde Hydrogenation. *J. Catal.* **2021**, *399*, 162−169.

(44) Morin, C.; Simon, D.; Sautet, P. Chemisorption of Benzene on Pt(111), Pd(111), and Rh(111) Metal Surfaces: A Structural and Vibrational Comparison from First Principles. *J. Phys. Chem. B* **2004**, *108*, 5653−5665.

(45) Brown, S. T.; Buitrago, P.; Hanna, E.; Sanielevici, S.; Scibek, R.; Nystrom, N. A. In *Bridges-2: A Platform for Rapidly-Evolving and Data Intensive Research*, Practice and Experience in Advanced Research Computing; ACM Digital Library, 2021; p 1.

(46) Towns, J.; Cockerill, T.; Dahan, M.; Foster, I.; Gaither, K.; Grimshaw, A.; Hazlewood, V.; Lathrop, S.; Lifka, D.; Peterson, G. D.; et al. Xsede: Accelerating Scientific Discovery. *Comput. Sci. Eng.* **2014**, *16*, 62−74.